RSC Advances

ROYAL SOCIETY OF CHEMISTRY

PAPER

View Article Online
View Journal | View Issue

Cite this: *RSC Adv.*, 2024, **14**, 8885

Phenothiazine appended thiophene derivative: a trilateral approach to copper ion detection in living cells and aqueous samples†

Mohan Ilakiyalakshmi and Ayyakannu Arumugam Napoleon *

This research paper unveils a fluorescent probe (**PTZ-SCN**) engineered for the specific detection of Cu^{2+}, featuring a 10-ethyl-10*H*-phenothiazine-3-carbaldehyde and 2-(thiophen-2-yl) acetonitrile moiety. The fluorescence sensing behavior of **PTZ-SCN** towards various metal cations was scrutinized in CH_3CN : HEPES (9 : 1) buffer aqueous solution. The UV absorbance of **PTZ-SCN** displayed a distinct red shift in the presence of Cu^{2+} cations, whereas other metal cations did not cause any interference. Similarly, the fluorescence emission of the probe was also only quenched by Cu^{2+} cations. The limit of detection (LOD) was calculated as 1.0461×10^{-8} M. **PTZ-SCN** showed the ability to identify Cu^{2+} using the colorimetric method, the fluorometric method and even through visual observation in a trilateral detection. We studied the recognition mechanism of **PTZ-SCN** for Cu^{2+} using ^{1}H-NMR, HRMS analysis, and time-dependent density functional theory (TDDFT) calculations. Furthermore, our study encompassed the investigation of **PTZ-SCN**'s practical applicability, bridging the gap from research to real-world implementation. This was achieved by employing test strips and water samples for the detection of Cu^{2+}. Additionally, the **PTZ-SCN** probe's low cytotoxicity and effective imaging properties for Cu^{2+} in living cells were confirmed, indicating that **PTZ-SCN** shows the potential to serve as a promising probe for detecting Cu^{2+} *in vivo*.

Received 7th November 2023
Accepted 22nd February 2024

DOI: 10.1039/d3ra07608c

rsc.li/rsc-advances

1 Introduction

The transition metal copper (Cu^{2+}) ion is the third most abundant element in the human body and is vital for a wide array of biochemical and physiological functions. It plays vital roles in the human body, including iron metabolism, neurotransmitter synthesis, connective tissue formation, melanin production, antioxidant defense, enzymatic reactions, bone and cardiovascular functions,[1] and thyroid regulation. Cu^{2+} is an essential cofactor for various enzymes involved in biochemical reactions such as cytochrome c oxidase, tyrosinase, and Cu superoxide dismutase. Additionally, recent findings have indicated its role in regulating cancer cell growth by triggering oncogenic BRAF mutations. The importance of copper for humankind is undeniable, but an overabundance or imbalance can result in serious effects, such as Alzheimer's,[2] Parkinson's,[3] Menkes,[4] Huntington,[5] Prion,[6] and Wilson diseases,[7] as well as having harmful effects on the kidneys and liver. Copper serves a multitude of industrial purposes such as building construction, renewable energy sources, electrical equipment, catalysts for alcohol oxidation, and beyond. Uncontrolled utilization of copper ion in various activities and its inadequate disposal can have direct ecological impacts and can pose risks to human health.[8,9] With a focus on sustainability and human well-being, the World Health Organization has set a safe copper range of 1.3 to 2 ppm for drinking water. The toxicity of copper affecting animals,[10] humans, and the environment is a matter of great concern among scientists. Therefore, the priority is to develop an effective technique using budget-friendly materials that can detect even trace amounts of Cu^{2+} in real-time samples.

Colorimetric and fluorometric sensing methods as optical detection techniques have become the leading approach for detecting metal ions due to their remarkable advantages including high selectivity, ease of use, visual clarity, instant response time, and on-field portability. Sensors with fluorogenic responses have been extensively studied because of their distinctive and facile identification of signal responses. Several metal ions are recognized as fluorescence quenching (turn-off) owing to their paramagnetic nature (*e.g.*, Cu^{2+}).[11–13] Over the past few decades, a significant number of research publications have focused on fluorescent chemosensors capable of detecting Cu^{2+} with a turn-off response.[14] These chemosensors encompass rhodamine,[15] quinoline,[16] curcumins,[17] and calixarenes.[18] These compounds have chemosensors that need specialized synthetic methods. The remarkable optical properties of phenothiazine derivatives have led to extensive research into their applications in diverse biological activities and metal ion detection.[19]

Thus, in such a context, we successfully synthesized the phenothiazine-thiophene acetonitrile compound **PTZ-SCN**

Department of Chemistry, School of Advanced Sciences, Vellore Institute of Technology, Vellore-632014, Tamil Nadu, India. E-mail: aanapoleon@vit.ac.in

† Electronic supplementary information (ESI) available. See DOI: https://doi.org/10.1039/d3ra07608c

through a simple Knoevenagel condensation reaction.[20,21] The newly synthesized **PTZ-SCN** demonstrated sensitivity and selectivity towards Cu^{2+} in both simulated physiological conditions (CH_3CN : HEPES buffer) and within cells. **PTZ-SCN** and **PTZ-SCN-Cu^{2+}** were examined by various techniques. The photophysical properties of both the ligand and complex were thoroughly characterized in the results and discussion section. Noteworthily, the **PTZ-SCN** probe proved to have very low cytotoxicity, making it viable for *in vivo* applications.

2 Experimental techniques

2.1 Materials and instruments

Phenothiazine, ethyl bromide, potassium tertiary butoxide, phosphorus oxychloride, dimethyl formamide, dimethyl formamide, chloroform, thiophene acetonitrile, piperidine, ethanol, and metal salts were purchased from suppliers including Sigma-Aldrich, TCI Chemicals, and SD-Fine Chem Ltd. Milli-Q water was used throughout the analytical investigation. Using a Bruker 400 MHz spectrometer, the ^{1}H-NMR (400 MHz) and ^{13}C-NMR (100 MHz) spectra of **PTZ-SCN** were captured with deuterated dimethyl sulfoxide and standard tetramethyl silane (TMS) as a reference to determine chemical shift (δ) values in parts per million units. The molecular mass of the **PTZ-SCN** and **PTZ-SCN-Cu^{2+}** was verified by acquiring HRMS spectra through the WATER-XEVO G2XS-QT instrument. The absorption and emission spectra were captured under room temperature using a 2 cm^2 cuvette in CH_3CN : HEPES buffer (9 : 1, v/v) medium on an Agilent 8543 UV spectrophotometer and Edinburg FLS 980 spectrometer, respectively. Live HeLa cells were performed for bioimaging using a fluorescence microscope.

2.2 Synthesis of PTZ-SCN

The earlier reported procedures were performed for the synthesis of **Et-PTZ** and **Et-PTZ-1-CHO**.[22]

Et-PTZ-1-CHO (0.1 g), thiophene acetonitrile (0.041 mL), and piperidine were dissolved in 15 mL of ethanol and the mixture was stirred overnight. After the crude sample was poured into ice, the reaction mixture was filtered using Whatman filter paper. Water was used to rinse the filter paper several times to thoroughly eliminate all remnants of the starting material. Finally, the product was dried. The **PTZ-SCN** product exhibited a vivid orange fluorescence and achieved a substantial yield of 92% (Scheme 1).

Comprehensive characterization of the **PTZ-SCN** probe was accomplished through the application of IR, NMR, and HRMS techniques. FT-IR cm^{-1}: CN stretching (2210) and C=C stretching (1571) (Fig. S1†). ^{1}H-NMR (400 MHz, DMSO) δ (ppm): 7.8 (d, J = 6.6 Hz, 1H), 7.6 (m, 3H), 7.3 (d, J = 4.4 Hz, 1H), 7.2 (m, 1H), 7.13 (m, 3H), 7.05 (d, J = 7.9 Hz), 6.9 (t, 1H), 3.9 (q, 3H) and 1.3 (t, 3H). The ^{13}C NMR spectrum of **PTZ-SCN** recorded at 400 MHz in DMSO-d$_6$ reveals distinct peaks at δ (ppm) values of 146.58, 143.39, 139.27, 139.26, 129.63, 128.41, 127.84, 127.72, 127.63, 127.60, 126.49, 123.61, 123.11, 122.09, 117.86, 116.23, 115.76, 102.28, 41.94, 40.61, 40.40, 40.20, 39.99, 39.78, 39.57, 39.36, and 12.93 (Fig. S2 and S3†). Furthermore, the High-Resolution Mass Spectrometer (HRMS) was used to verify the consistency between the observed data (360.075) and the calculated mass (360.075) of the **PTZ-SCN** compound (Fig. S4†).

2.3 General procedures

2.3.1 Preparation of the PTZ-SCN stock solution. UV absorption and FL emission spectral studies were investigated in an aqueous solution with CH_3CN : HEPES buffer (9 : 1, v/v) mixture, which contained the probe **PTZ-SCN** at a concentration of 1×10^{-6} M. Double distilled water was used to prepare stock solutions of cations (Ag^+, Ba^{2+}, Co^{2+}, Cd^{2+}, Zn^{2+}, Fe^{2+}, Hg^{2+}, Li^{2+}, Mg^{2+}, Mn^{2+}, Pb^{2+}, Sr^{2+}, Fe^{3+}, Al^{3+}, and Cu^{2+}) at a concentration of 1×10^{-6} M. To obtain a concentration of 1×10^{-6} M for the sensor compound **PTZ-SCN**, a stock solution was prepared by mixing acetonitrile and HEPES buffer in a 9 : 1 ratio. A preliminary investigation was carried out to assess the selective reactivity of the **PTZ-SCN** probe towards various analytes, with a primary focus on observing color variations.

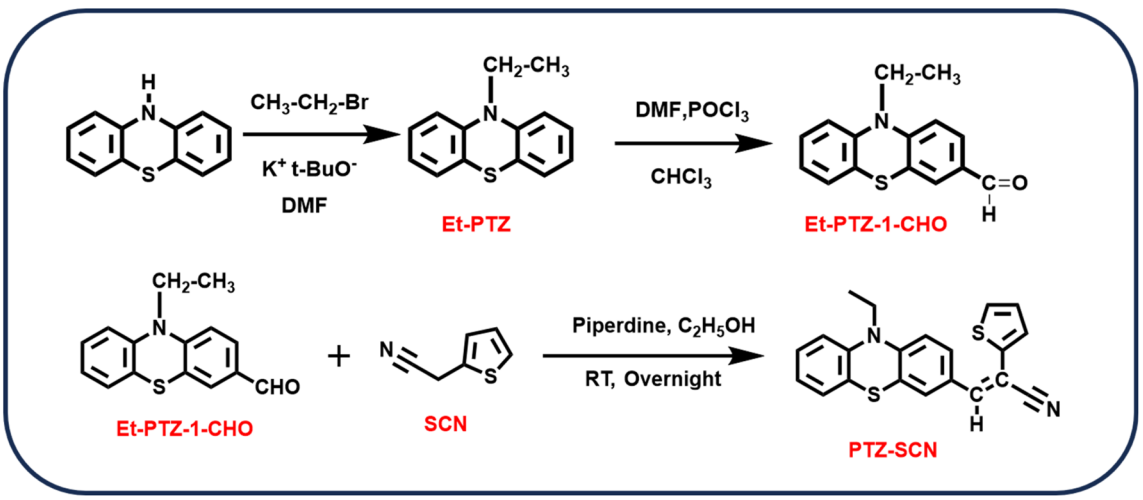

Scheme 1 Synthesis of the PTZ-SCN probe.

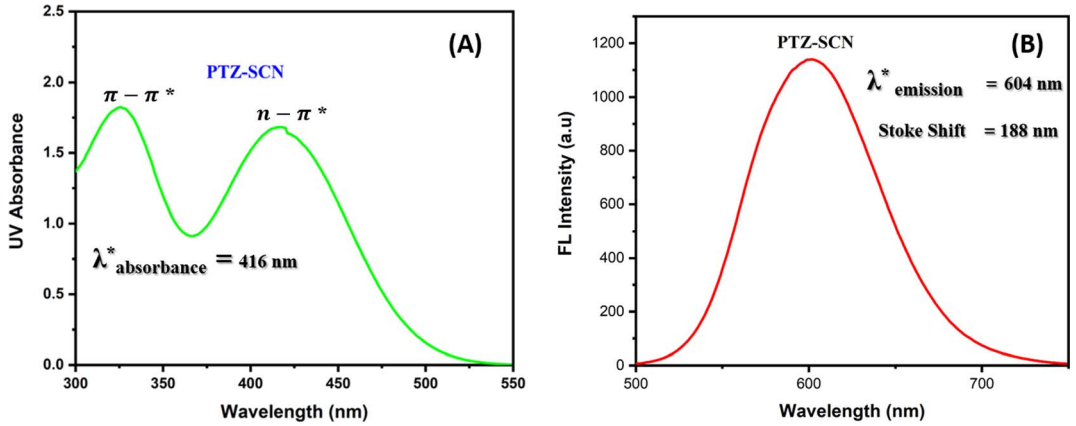

Fig. 1 (A) UV absorption spectra of PTZ-SCN in an acetonitrile solvent. (B) PTZ-SCN displays a Stoke's shift of 188 nm in its emission spectrum.

This research explored the effect of pH using a HEPES buffer solution. A sequence of pH solutions covering the range from 2 to 12 was established by mixing 0.1 M H_3PO_4 and 0.1 M NaOH while ensuring a consistent total ionic strength at 0.1 ± 0.01 M.

2.3.2 Computational studies. Density functional theory (DFT) was applied to theoretically evaluate the structure and functional groups of the synthesized compounds. The choice of a basic set in DFT calculations enhances the accuracy in characterizing the bonding nature of metal ions, charge distributions, and molecular orbitals. Using B3LYP calculations in both gas and liquid phases, we theoretically examined the geometries of **PTZ-SCN**, prior to and following their interaction with the cupric ion. The 6-311G (d,p) basic sets were employed for the atoms (nitrogen, sulfur, hydrogen, and carbon) in our computational work. Furthermore, calculations were performed to determine the energy band gap values of **PTZ-SCN** and their states after interacting with cupric ions. The G16 package was employed in our study for theoretical investigations, while electronic geometries and frontier molecular orbital data were extracted using Gauss View 6.1.1.

2.3.3 MTT assay protocol. HeLa (human cervical cancer cell line) cells were placed discretely in 96-well plates, with each well containing 50 000 cells. The culture medium was supplemented with 10% Fetal Bovine Serum (FBS), penicillin, and streptomycin, and the cells were incubated in a humidified atmosphere with 5% CO_2 at 37 °C. After being washed with 200 μL of 1× PBS, the cells were subjected to a 24 hour incubation in serum-free media, during which they were treated with different concentrations of **PTZ-SCN** (10, 20, 30, 40, 50, 60, 70, 80, 90, and 100 μg mL^{-1}). In addition, we treated the cells with 0.5 mg mL^{-1} MTT dissolved in 1× PBS and incubated the mixture for three hours. Subsequently, the MTT solution was aspirated and the cells were rinsed with 100 μL of PBS and the formed crystals were combined with 100 μL of DMSO solution.

3 Results and discussion

3.1 Absorption and fluorescence studies

The UV absorption spectrum of the **PTZ-SCN** probe was meticulously recorded within an acetonitrile solvent at a concentration of 1×10^{-6} M, revealing a conspicuous peak at 416 nm, as depicted in Fig. 1A. Fig. 1B unveils the fluorescence emission spectrum of the **PTZ-SCN**, where a distinct emission maximum is at 604 nm. The luminescent nature of the **PTZ-SCN** probe finds its determination through the Stoke's shift value, which can be calculated from the difference between the maxima emission and absorption values of the **PTZ-SCN** (eqn (1)). The probe presents an appreciably elevated Stoke's shift value at 188 nm (Table 1).

$$\Delta\lambda_{Stoke} = \lambda_{max.\ emission} - \lambda_{max.\ absorption} \quad (1)$$

Table 1 Complete photophyscial data of PTZ-SCN

S. no.	Property	Absorption spectra	Fluorescence spectra
1	Optical characteristics	UV active	FL active
2	Analysis technique	Ultraviolet-visible spectrophotometer	Fluorescence spectrophotometer
3	Solvent utilized	Acetonitrile	Acetonitrile
4	Probe concentration	(1×10^{-6} M)	(1×10^{-6} M)
5	Wavelength (λ_{max})	416 nm	604 nm
6	Cation detected	Cu^{2+}	Cu^{2+}
7	Concentration of cation	(1×10^{-6} M)	(1×10^{-6} M)
8	Spectral shift	Redshift	Quenching nature
9	The stoichiometric ratio of **PTZ-SCN** : Cu^{2+}	1 : 1	1 : 1
10	Limit of detection (LOD)	7.8089×10^{-6} M	1.0461×10^{-8} M
11	pH stability	pH = 2 to 12	pH = 2 to 12

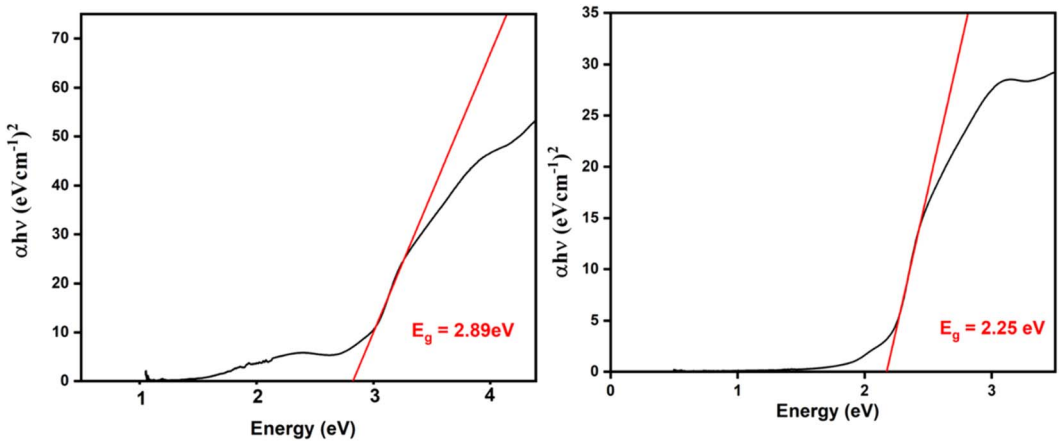

Fig. 2 A comparative examination of Tau's plot for the PTZ-SCN probe and PTZ-SCN-Cu^{2+} complex.

$$h\nu = A(h\nu - E_g) \quad (2)$$

The band gap of the **PTZ-SCN** and **PTZ-SCN-Cu^{2+}** probes was determined by the energy gap that exists between the highest occupied molecular orbital (HOMO) and the lowest occupied molecular orbital (LUMO) (Fig. 2). By employing eqn (2), the optical band gaps of the probes were determined. This plot helps determine the band gap by identifying the point where the absorption peak begins using straight-line interpolation. The band gap of the **PTZ-SCN-Cu^{2+}** complex is 2.25 eV less than that of the **PTZ-SCN** probe, which records a band gap of 2.89 eV.

3.2 UV-visible spectral response of PTZ-SCN to metal ions

The selectivity assessment of the **PTZ-SCN** probe involved employing visual color changes, along with colorimetric UV-visible and FL spectroscopy techniques. The various metal ions including Ag^{+}, Ba^{2+}, Co^{2+}, Cd^{2+}, Zn^{2+}, Fe^{2+}, Hg^{2+}, Li^{2+}, Mg^{2+}, Mn^{2+}, Pb^{2+}, Sr^{2+}, Fe^{3+}, Al^{3+}, and Cu^{2+} (15 metals) were tested within an CH_3CN : HEPES buffer (9 : 1, v/v) system.[23,24] The

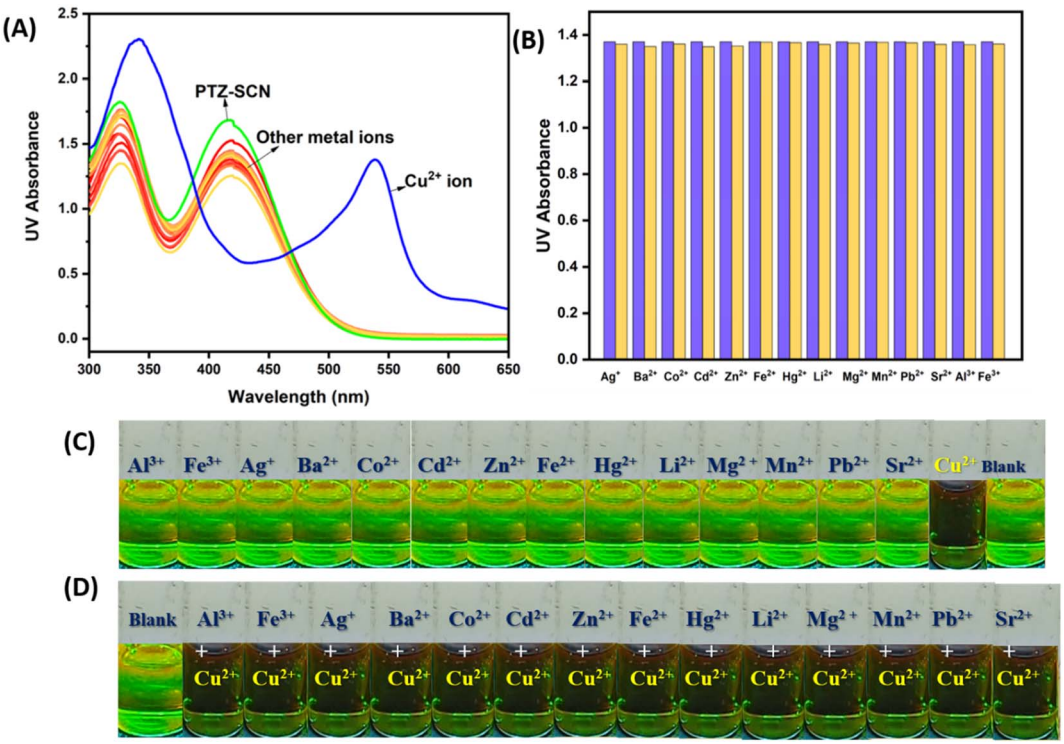

Fig. 3 (A) The effect of metal ions on absorbance responses in PTZ-SCN. (B) The impact of Cu^{2+} on absorbance changes at 538 nm amidst a variety of metal ions. (C) Visualization of PTZ-SCN following the introduction of different metal ions. (D) The absorbance image of PTZ-SCN upon adding Cu^{2+} with other metal ions under UV light (short wavelength = 254 nm).

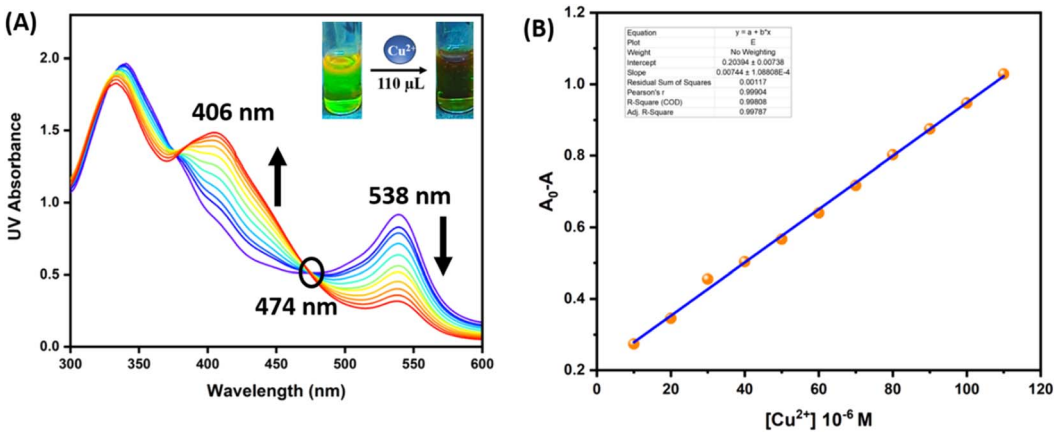

Fig. 4 (A) Investigation of the UV titration of PTZ-SCN with Cu^{2+} at various concentration levels. (B) Calibration plot of PTZ-SCN of UV titration.

solution of the **PTZ-SCN** was a yellow color. Remarkably, when Cu^{2+} (10 eq.) was added to the solution **PTZ-SCN**, a new notable peak emerged at 538 nm (Fig. 3A), causing the solution to shift from yellow to reddish-brown. In contrast, when the same conditions were applied to the addition of the remaining 12 metal ions individually, negligible changes in absorbance within the visible spectrum were observed, and the solution retained the color of the blank control under UV light (Fig. 3C). To examine **PTZ-SCN**'s ability towards anti-interference, the shift in absorbance of **PTZ-SCN** solution upon introducing Cu^{2+} (10 eq.), along with different metal ions was measured. Fig. 3B displays that the introduction of diverse metal ions exhibited minimal impact on the absorbance at 538 nm. Furthermore, the color transformation to reddish-brown was observed in the solutions of other metal ions upon the addition of the Cu^{2+} (Fig. 3D). These findings demonstrate that the presence of other metal ions did not influence the detection of Cu^{2+} by **PTZ-SCN**, underscoring **PTZ-SCN**'s remarkable anti-interference properties.

PTZ-SCN exhibits a colorimetric response to Cu^{2+} in a CH_3CN/HEPES buffer solution, and we subsequently investigated its sensitivity for detecting Cu^{2+}. In the titration process, with the incremental addition of Cu^{2+} to **PTZ-SCN**, the 406 nm band exhibited a gradual increase. Simultaneously, a new band appeared at 538 nm, leading to a gradual decrease in the original band and a transition from yellow to reddish-brown

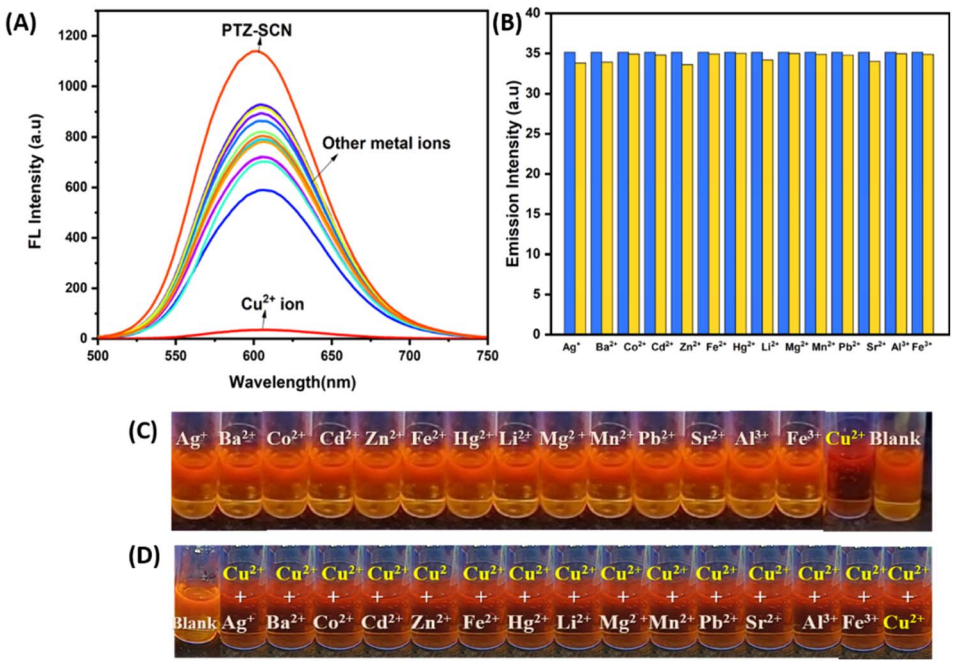

Fig. 5 (A) The fluorescence spectral changes of PTZ-SCN induced by different metal ions. (B) Interference study of PTZ-SCN's response to Cu^{2+} among other cations. (C) Visible fluorescence change of PTZ-SCN upon Cu^{2+} introduction under UV light (long wavelength = 365 nm). (D) Interference image of PTZ-SCN-Cu^{2+} with other metal ions under UV light (long wavelength = 365 nm).

(Fig. 4A). The development of a unique isosbestic point at 474 nm affirmed the formation of a single metal complex. As a result, a linear increase in absorbance at 406 nm was observed with the rising concentration of Cu^{2+} in the range of 0–110 μL. Additionally, the absorbance ratio (A_{406}/A_{538}) demonstrated a linear correlation in the calibration plot and the limit of detection (LOD) was determined to be 7.8089×10^{-6} M (Fig. 4B).[25] Furthermore, the plot displayed excellent linearity with an R^2 value of 0.99984, indicating **PTZ-SCN**'s capability to monitor Cu^{2+}, even at low concentrations (Fig. 8B).

3.3 Fluorescence spectral response of PTZ-SCN to metal ions

The **PTZ-SCN** was examined using a fluorescence spectrophotometer at a concentration of 1×10^{-6} M in the CH_3CN : HEPES buffer (9 : 1, v/v) system. The fluorescent spectrum analysis reaffirmed **PTZ-SCN** selectivity for Cu^{2+}.[26] As depicted in Fig. 5A, **PTZ-SCN** exhibited a significant emission peak at 604 nm. The color of the **PTZ-SCN** solution was distinctly orange. Notably, the addition of 10 equivalents of Cu^{2+} to the **PTZ-SCN** solution caused quenching, resulting in a shift from orange to reddish-brown. On the other hand, the same conditions applied to the remaining 12 metal ions individually resulted in minimal alterations in emission, and the solution maintained the same color as the blank control (Fig. 5C). To evaluate the anti-interference properties of **PTZ-SCN**, we measured the change in emission of its solution upon adding Cu^{2+} (10 eq.) along with different metal ions (Fig. 5B).[27,28] The interference test revealed that the introduction of various metal ions had a negligible effect on the emission at 600 nm. Additionally, the introduction of Cu^{2+} led to a noticeable transformation in the color of the solutions containing different other metal ions, turning them a reddish-brown color (Fig. 5D). These findings illustrate that the presence of different metal ions did not affect the ability of **PTZ-SCN** to detect Cu^{2+}, emphasizing its outstanding anti-interference properties.

Subsequently, the fluorescence sensitivity of **PTZ-SCN** to Cu^{2+} was examined within the CH_3CN : HEPES buffer (9 : 1, v/v) system. As depicted in Fig. 6A, the fluorescence intensity at 604 nm exhibited a gradual decrease, leveling off once the Cu^{2+} concentration reached 90 μL. The emission intensity was found to be linearly dependent on Cu^{2+} concentration within the 0–90 μL range, resulting in the linear regression value $R^2 = 0.9993$ (Fig. S6†)[29] with a calculated limit of detection of 1.0461×10^{-8} M (Fig. 6B).

3.4 Kinetic analysis and pH effects on sensor PTZ-SCN

The response time of **PTZ-SCN** was determined through fluorescence measurements taken at distinct time intervals after the addition of Cu^{2+} at different concentrations. At the outset, a rapid decrease in intensity was noticeable for all Cu^{2+} concentrations within the first 20 seconds, with subsequent stabilization of the fluorescence signals lasting until the 90th second (Fig. 7A). In comparison to other probes utilized for the same Cu^{2+} analyte, **PTZ-SCN** displays a markedly shorter time response.[30] These findings demonstrate the **PTZ-SCN** probe's suitability for real-time monitoring of Cu^{2+}.

pH is a vital parameter that has a substantial impact on fluorescence measurements. Fig. 7B and S8† display the response of the **PTZ-SCN** sensor to varying levels of acidic and alkaline conditions. **PTZ-SCN**'s emission intensity remains constant as the pH ranges from 2 to 12, revealing the stability of **PTZ-SCN** across a broad pH range.[31,32] The **PTZ-SCN** probe is extensively utilized in biological systems due to its remarkable stability in both acidic and alkaline conditions. Hence, the results suggest that **PTZ-SCN**'s wide pH detection range renders it a reliable choice for application in biological contexts.

3.5 Binding mechanistic pathway PTZ-SCN probe

The stoichiometric binding ratio of **PTZ-SCN** with Cu^{2+} was ascertained using a Job's plot, involving molar fractions ranging from 0.1 to 0.9. From the mole fraction value of 0.5, we can conclude that there is a 1 : 1 binding ratio between Cu^{2+} and the **PTZ-SCN** probe[33] (Fig. 8A and S7†). The binding constant, determined to be 4.6071×10^4 M^{-1}, was acquired through the utilization of the Benesi–Hildebrand equation (Fig. 8B and S6†).

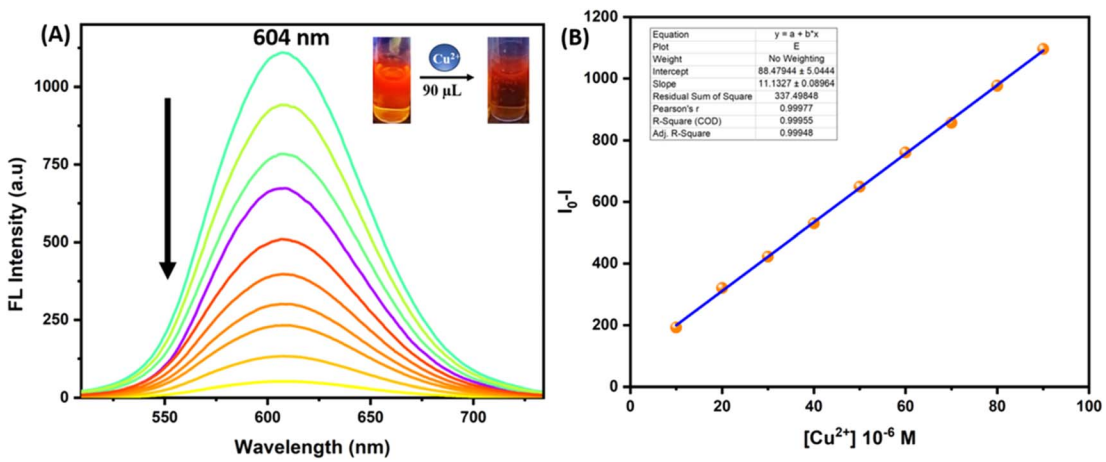

Fig. 6 (A) FL spectral titration investigation of the PTZ-SCN with Cu^{2+} concentration ranging from 0–90 μL. (B) Calibration plot of FL titration.

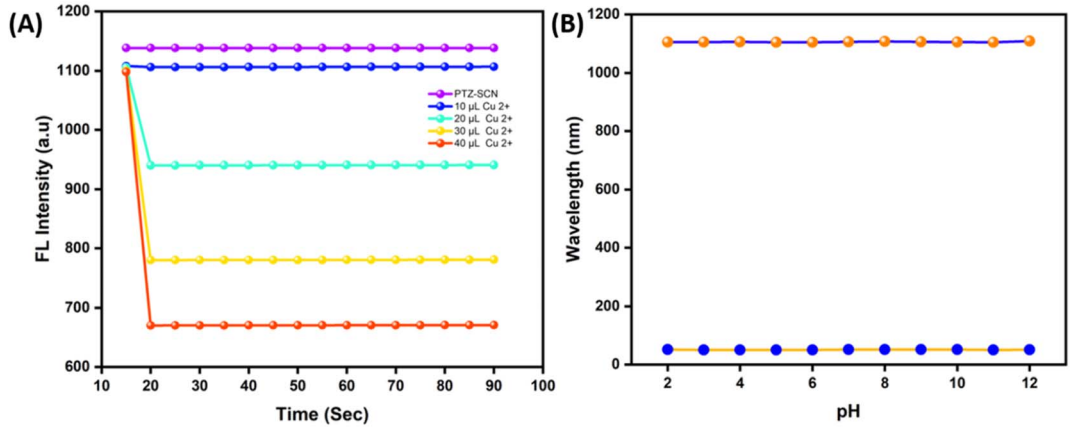

Fig. 7 (A) Time response of the PTZ-SCN sensor to Cu^{2+}. (B) pH effect of PTZ-SCN and PTZ-SCN-Cu^{2+} on the emission spectrum.

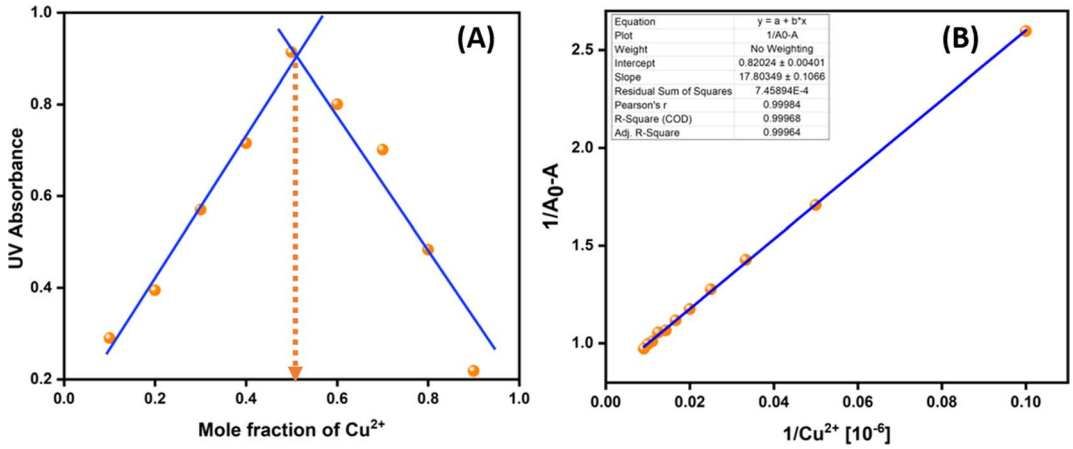

Fig. 8 (A) Job's plot. (B) B–H plot of PTZ-SCN in the incremental concentration of cupric ions.

Additional validation was substantiated by employing Electron Spray Ionization Mass Spectroscopy, yielding a recorded mass of 426.04, in remarkable congruence with the anticipated mass of 424.04 mass/number of charged ions (Fig. S5†).

The emission intensity at 604 nm diminishes upon the introduction of Cu^{2+} and this phenomenon is associated with Cu^{2+} paramagnetic quenching effect. Being a paramagnetic ion with an empty d-shell, Cu^{2+} is widely recognized for its powerful ability to inhibit fluorophore emission through a photoinduced transfer of electrons or energy from the metal to the fluorophore[34] (Fig. 9). In order to elucidate the binding mode between **PTZ-SCN** and cupric (Cu^{2+}) ions, we conducted ^{1}H-

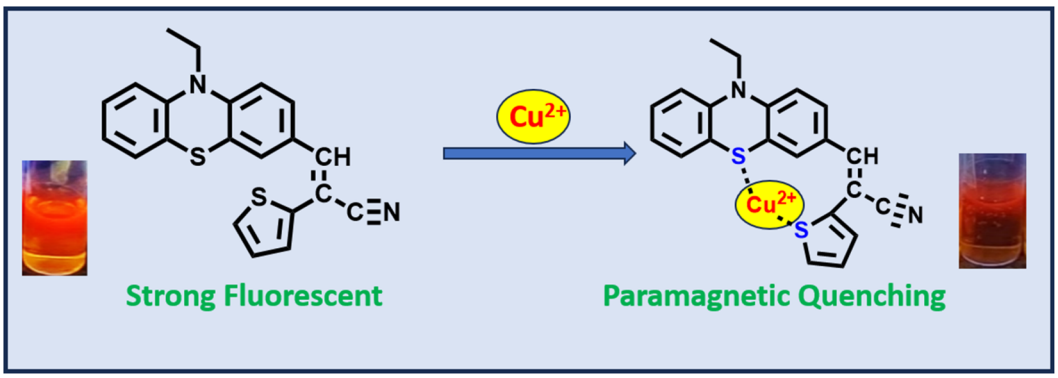

Fig. 9 Proposed sensing mechanism.

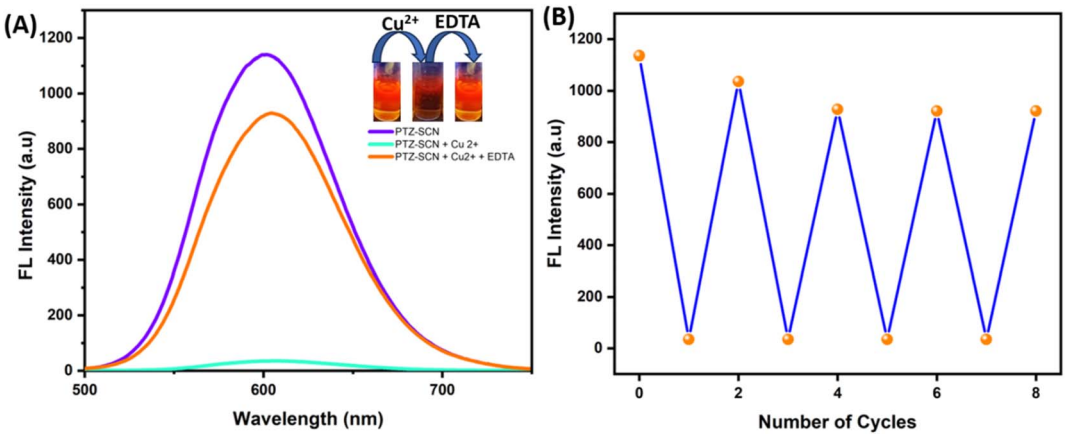

Fig. 10 (A) Reusability of PTZ-SCN with an EDTA. (B) Tracking the number of repetitive cycles triggered by Cu^{2+} in PTZ-SCN.

NMR titration experiments in DMSO-d_6, as shown in Fig. S9.† We tracked the changes in chemical shifts caused by cations, which were quantified as the mole ratio (Cu^{2+}/**PTZ-SCN**) from 0 to 1 equivalent. The aromatic hydrogens (ArH) demonstrated a minor downfield displacement in chemical shifts when Cu^{2+} was introduced. The H-signal attributed to thiophene became broader and weaker. These results suggest a connection between the sulfur atoms in thiophene and phenothiazine when binding with Cu^{2+}.

3.6 Reusability of the PTZ-SCN probe

The **PTZ-SCN-Cu^{2+}** complex probe's reusability is attained by incorporating EDTA (ethylenediamine tetra acetic acid). EDTA addition had no discernible influence on the emission spectra of the **PTZ-SCN** solution, but it induced a marked change in fluorescence in the **PTZ-SCN-Cu^{2+}** solution. Emission spectroscopy was employed to investigate the reversible sensing characteristics of **PTZ-SCN** throughout four distinct sequences, initiated by the Cu^{2+} addition and subsequently followed by EDTA. When EDTA was introduced to the **PTZ-SCN-Cu^{2+}** complex, the emission peak was quenched at 604 nm, signifying the release of free **PTZ-SCN**. Interaction between free **PTZ-SCN** and Cu^{2+} resulted in the development of the **PTZ-SCN-Cu^{2+}** complex, which displayed quenching fluorescence at 604 nm (Fig. 10A). Sequentially introducing the cupric ion and EDTA over four cycles resulted in emission shifts, encompassing both enhanced and quenched transitions. During those four cycles, it was evident that the transition in fluorescence emission had reversed, leading to a change in the color of fluorescence[35] (Fig. 10B). From the analysis previously mentioned, it was apparent that the **PTZ-SCN** probe could undergo recycling and be reused effectively.

3.7 Density functional theory

We conducted a comprehensive density functional theory (DFT) study, optimizing the mechanistic structures of both **PTZ-SCN** and **PTZ-SCN-Cu^{2+}** in the gas and liquid phases using Becke's three-parameter Lee–Yang–Parr (B3LYP)/6-31 + G** basic set.[36] The 6-31 + G** basic set was selectively employed for atomic species like C, H, S, and N.[37,38] Theoretical investigations through DFT studies (Fig. 11) were conducted to explore the 3D-computed structures and energy levels of both the **PTZ-SCN** and **PTZ-SCN-Cu^{2+}** compounds. The dihedral angle of S–Cu–S measures 69.315°, indicating the structural arrangement of the complex. The **PTZ-SCN-Cu^{2+}** complex displayed a calculated interaction energy of −3347.521213 Hartree, affirming the stability conferred by the coordination bond.

Free **PTZ-SCN** exhibited the highest occupied molecular orbital (HOMO) with electron density uniformly distributed throughout the molecules, while the lowest unoccupied

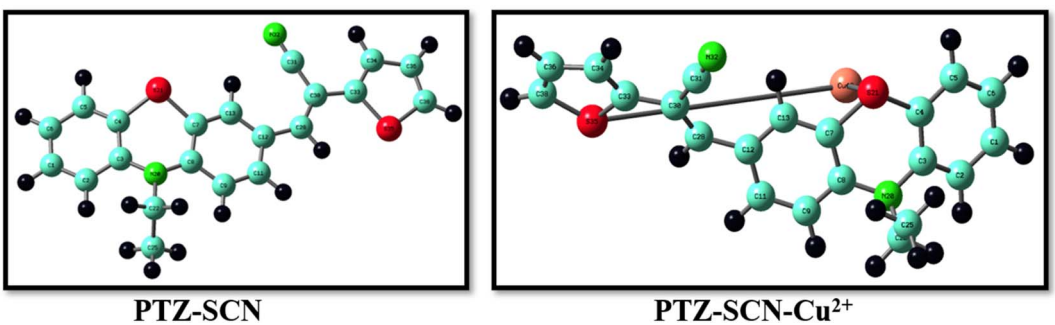

Fig. 11 Structural optimization of PTZ-SCN and binding with Cu^{2+}.

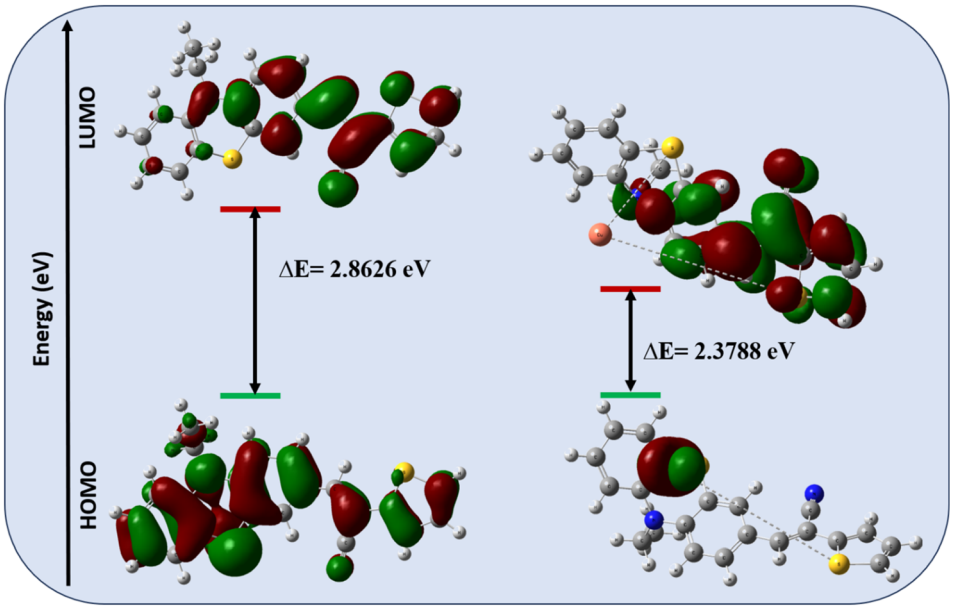

Fig. 12 Frontier molecular orbital and band energies of PTZ-SCN and PTZ-SCN-Cu^{2+}.

molecular orbital (LUMO) showcased electron density focused primarily in the thiophene acetonitrile region. Consequently, it provides a compelling depiction of intramolecular charge transfer (ICT) dynamics, specifically involving electron transfer from the highest occupied molecular orbital (HOMO) to the lowest unoccupied molecular orbital (LUMO).[39,40] Within the **PTZ-SCN-Cu^{2+}** complex, it is evident that the HOMO's electron density is localized around the metal ion, while the LUMO's electron density predominantly resides within the thiophene moiety, potentially mitigating any intramolecular charge transfer between thiophene acetonitrile and phenothiazine (Fig. 12). This study provides clear evidence of copper-mediated intramolecular charge transfer in the **PTZ-SCN-Cu^{2+}** complex, as supported by the diminished band gap of 2.378 eV, notably lower than that of **PTZ-SCN** at 2.862 eV.

PTZ-SCN was subjected to TD-DFT calculations in the acetonitrile solvent phase, employing B3LYP with a 6–31 + G** level of theory. Fig. S10† provides a theoretical UV-visible spectra, whereas Fig. 3a displays the experimental spectra of **PTZ-SCN**. The shift from n–π* to intramolecular charge transfer transitions was confirmed experimentally, with the observed wavelength at 416 nm matching the theoretical value of 498 nm. In contrast to experimental findings, the solvent demonstrates a red shift due to its comparatively lesser influence on theoretical investigations. **PTZ-SCN** exhibits a major distribution of electronic energy in higher energy states, specifically through transitions H−2 → L (64.5%) and H → L (93.7%) (Table S1†).

3.8 Practical applications

3.8.1 Paper test strips: a resourceful tool in practice. A practical demonstration of an immediate sensing response was carried out with paper-based test strips. The test strip analysis was initiated by cutting Whatman filter papers into equally sized portions and immersing them in an acetonitrile solution containing **PTZ-SCN** (10 μM) for approximately 3 minutes, followed by air drying.[41] A color change was observed upon the addition of a precise amount of 5 μM of the corresponding cation solution to the strip. Our meticulous observation has been documented and is visually represented in Fig. S11.† These images clearly illustrate that paper test strips containing the **PTZ-SCN** can effectively detect Cu^{2+}, even at concentrations as low as ≤10 μM, in aqueous solutions, resulting in an immediate color transition from yellow to reddish-brown.

3.8.2 Real water samples. The **PTZ-SCN** probe's real-world utility was demonstrated through its ability to capture Cu^{2+} in diverse real water samples. Water samples were collected from different areas of the Ranipet district, Tamil Nadu, which had been spiked with differing amounts of Cu^{2+}. Under standardized sensing procedures, we introduced Cu^{2+} at various known concentrations into these samples.[42–44] The observable data provides strong evidence that the **PTZ-SCN** probe was more proficient at detecting Cu^{2+} in the diverse water samples collected. The experiment was meticulously repeated thrice to affirm the results, which are comprehensively detailed in Table S2.† The results provide evidence of the **PTZ-SCN** probe's practical utility in continuous real-time monitoring analysis of various environmentally polluted water samples.

3.9 Cell viability analysis and emerging bioimaging techniques

The biocompatibility of the **PTZ-SCN** probe is a fundamental factor in the realm of practical biological applications. To assess the impact of the **PTZ-SCN** probe, a cytotoxicity test was conducted on HeLa cells using the MTT method.

The viability of cervical cells remained intact in over 92% of cases after exposure to **PTZ-SCN** at concentrations from 0 to 100

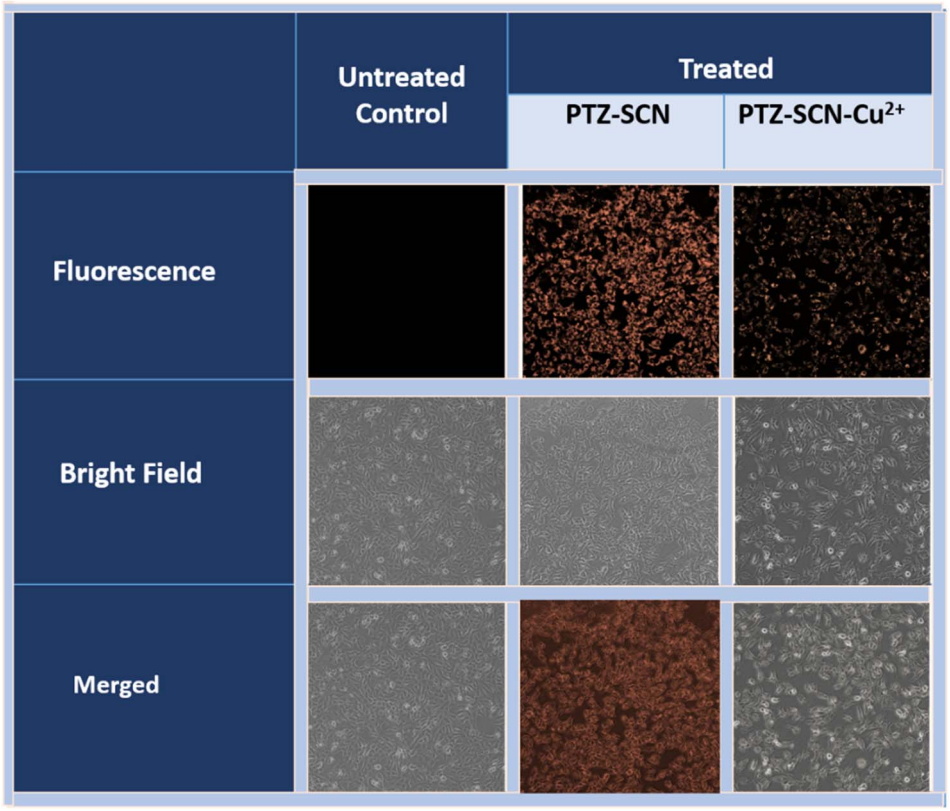

Fig. 13 Fluorescent imaging of cervical cancer cells post-incubation with PTZ-SCN and PTZ-SCN-Cu^{2+}.

μM for 24 hours, indicating the compound's remarkable non-toxic nature and favorable cell viability.[45] *In vitro* analysis demonstrated the excellent bio-imaging potential of **PTZ-SCN-Cu^{2+}** by revealing its exceptionally low cytotoxicity (Fig. S12†).

A biological application was carried out to monitor the presence of cupric ions and the **PTZ-SCN** within HeLa cells, capitalizing on the exceptional selectivity of the **PTZ-SCN** probe for detecting Cu^{2+}. Images of the cells were captured using fluorescence microscopy with an excitation wavelength of 416 nm. Fluorescence became apparent when **PTZ-SCN** was added to cells, even without external cupric ions, owing to its emission characteristics that enabled easy visualization through fluorescence microscopy. The existence of orange fluorescence in the fluorescent images confirmed that the cells had absorbed the **PTZ-SCN** over the incubation time. In contrast, the presence of 100 μM cupric ions in the preloaded cells led to a remarkable quenching of fluorescence when **PTZ-SCN** was introduced (Fig. 13). Thus, the bioimaging investigation substantiates the remarkable capability of the **PTZ-SCN** to detect cupric ions within biological environments without any adverse consequences.[46,47]

3.10 Comparison analysis

In order to emphasize the superior Cu^{2+} detection performance of the current **PTZ-SCN** probe, we evaluated its sensing properties in comparison to those of probes previously discussed in the literature (Table S3†). The **PTZ-SCN** compound stands out among known probes by offering trilateral detection methods for detection of Cu^{2+} naked-eye observation, colorimetry, and fluorometry. An all-encompassing table detailing various probes and their corresponding parameters clearly underscores the exceptional qualities of the **PTZ-SCN** probe. These attributes encompass specific selectivity, relative sensitivity, rapid response, and the lowest limit of detection (LOD).

4 Conclusion

In a nutshell, the synthesis of the **PTZ-SCN** probe, a highly efficient and easily accessible colorimetric and fluorometric chemosensor, was accomplished through the Knoevenagel condensation of phenothiazine and thiophene acetonitrile. The interaction between **PTZ-SCN** and cations was investigated *via* UV-visible and fluorescence techniques. The **PTZ-SCN** probe showed great sensitivity and a distinct response to Cu^{2+}, achieving a low limit of detection (LOD) of 1.0461×10^{-8} M in a linear range between 0–90 μL. The binding ratio of **PTZ-SCN** : Cu^{2+} (1 : 1) was confirmed with multiple techniques including Job's plot, B–H plot, ^{1}H NMR titration, TD-DFT, and HRMS spectroscopy. Moreover, our study was expanded to encompass an examination of **PTZ-SCN**'s practical feasibility through test strips, real water samples, and living cells.

Conflicts of interest

The authors disclose that they have no conflicts of interest.

Acknowledgements

Our sincere thanks to the Vellore Institute of Technology for their invaluable laboratory and instrumental support. We also acknowledge the support of DST-VIT-FIST for providing NMR and HRMS facilities.

References

1 A. M. Ghalibaf, S. S. Soflaei, G. A. Ferns, M. Saberi-Karimian and M. Ghayour-Mobarhan, *J. Trace Elem. Med. Biol.*, 2023, **80**, 127255.
2 K. P. Kepp and R. Squitti, *Coord. Chem. Rev.*, 2019, **397**, 168–187.
3 P. Dusek, P. M. Roos, T. Litwin, S. A. Schneider, T. P. Flaten and J. Aaseth, *J. Trace Elem. Med. Biol.*, 2015, **31**, 193–203.
4 S. G. Kaler, *J. Trace Elem. Med. Biol.*, 2014, **28**, 427–430.
5 L. M. Cordeiro, M. V. Soares, A. F. da Silva, L. V. dos Santos, L. I. de Souza, T. L. da Silveira, F. B. O. Baptista, G. V. de Oliveira, C. Pappis, V. L. Dressler, L. P. Arantes, F. Zheng and F. A. A. Soares, *Neurotoxicology*, 2023, **97**, 120–132.
6 W. Cerpa, L. Varela-Nallar, A. E. Reyes, A. N. Minniti and N. C. Inestrosa, *Mol. Aspects Med.*, 2005, **26**, 405–420.
7 D. Huster and S. Lutsenko, *Mol. BioSyst.*, 2007, **3**, 816–824.
8 W. P. Covre, S. J. Ramos, W. V. d. S. Pereira, E. S. de Souza, G. C. Martins, O. M. M. Teixeira, C. B. do Amarante, Y. N. Dias and A. R. Fernandes, *J. Hazard. Mater.*, 2022, **421**, 126688.
9 N. R. Pandit, S. Bej, R. Das, N. Ghosal, A. Mondal, R. Pal, M. Ghosh, P. Banerjee and B. Biswas, *Dalton Trans.*, 2023, **52**, 11130–11142.
10 E. A. B. Pajarillo, E. Lee and D. K. Kang, *Anim. Nutr.*, 2021, **7**, 750–761.
11 A. R. Kwilas, R. N. Donahue, K. Y. Tsang and J. W. Hodge, *Cancer Cell*, 2015, **2**, 1–17.
12 S. Sharma and K. S. Ghosh, *J. Mol. Struct.*, 2021, **1237**, 130324.
13 G. Tamil Selvan, C. Varadaraju, R. Tamil Selvan, I. V. M. V. Enoch and P. Mosae Selvakumar, *ACS Omega*, 2018, **3**, 7985–7992.
14 B. Naskar, R. Modak, D. K. Maiti, A. Bauzá, A. Frontera, P. K. Maiti, S. Mandal and S. Goswami, *RSC Adv.*, 2017, **7**, 11312–11321.
15 P. Ozmen, Z. Demir and B. Karagoz, *Eur. Polym. J.*, 2022, **162**, 110922.
16 S. Zhang, H. Zhang, L. Zhao, L. Xu, P. Ma, P. Ren and D. Song, *Spectrochim. Acta, Part A*, 2023, **284**, 121799.
17 B. Gogoi and N. Sen Sarma, *ACS Appl. Mater. Interfaces*, 2015, **7**, 11195–11202.
18 A. Lorente, A. Ochoa, J. Rodriguez-Lavado, S. Rodriguez-Nuévalos, P. Jaque, S. Gil, J. A. Sáez and A. M. Costero, *ACS Omega*, 2022, **8**, 819–828.
19 X. Lu, Y. Zhan and W. He, *J. Photochem. Photobiol., B*, 2022, **234**, 112528.
20 F. A. M. Al-Zahrani, K. A. Alzahrani, R. M. El-Shishtawy, K. Abu Mellah, A. M. Al-Soliemy and A. M. Asiri, *Luminescence*, 2020, **35**, 998–1009.
21 S. Wang, B. Zhang, W. Wang, G. Feng, D. Yuan and X. Zhang, *Chem.–Eur. J.*, 2018, **24**, 8157–8166.
22 M. Ilakiyalakshmi and A. A. Napoleon, *J. Photochem. Photobiol., A*, 2023, **447**, 115213.
23 L. Deng, L. Xue, Y. Gao, S. Fu and H. Wang, *Spectrochim. Acta, Part A*, 2024, **305**, 123479.
24 A. Hoque, M. Sanaul Islam, M. Mohammad, S. Khan, M. Maidul Islam, H. Al Rasid Gazi, E. Zangrando and M. Akhtarul Alam, *Inorg. Chim. Acta*, 2023, **557**, 121720.
25 N. Gao, M. Zhang and Y. Wang, *J. Mol. Struct.*, 2024, **1295**, 136670.
26 S. Kumar, B. Lal, R. K. Tittal, G. Singh, J. Singh, R. Sharma and J. K. Sabane, *Sens. Diagn.*, 2023, **2**, 1267–1276.
27 K. Y. Ryu, J. J. Lee, J. A. Kim, D. Y. Park and C. Kim, *RSC Adv.*, 2016, **6**, 16586–16597.
28 W. T. Guo, Y. F. Ding, X. Li, L. Tong, L. Dou and W. K. Dong, *Inorg. Chim. Acta*, 2023, **557**, 121704.
29 J. Isaad and A. El Achari, *J. Mol. Struct.*, 2021, **1228**, 129771.
30 X. Li, X. Liu and F. Li, *Spectrochim. Acta, Part A*, 2023, **304**, 123377.
31 M. Shahbaz, S. Sharif, M. Saeed, A. Ashraf and T. T. Rehman Afzal, *J. Lumin.*, 2023, **263**, 120149.
32 A. Mishra, A. Kushwaha, P. Maurya and R. Verma, *Spectrochim. Acta, Part A*, 2024, **305**, 123554.
33 J. C. Guirado-Moreno, I. Carreira-Barral, S. Ibeas, J. M. García, D. Granès, N. Marchet and S. Vallejos, *ACS Appl. Mater. Interfaces*, 2023, **15**, 16055–16062.
34 A. Singh, P. Yadav, S. Singh, P. Kumar, S. Srikrishna and V. P. Singh, *J. Mater. Chem. C*, 2023, **38**, 13056–13066.
35 W. C. Chan, M. P. Ng, C. W. Ang, K. S. Sim and K. W. Tan, *Inorg. Chim. Acta*, 2023, **557**, 121703.
36 V. A. Rassolov, J. A. Pople, M. A. Ratner and T. L. Windus, *J. Chem. Phys.*, 1998, **109**, 1223–1229.
37 G. A. Petersson, A. Bennett, T. G. Tensfeldt, M. A. Al-Laham, W. A. Shirley and J. Mantzaris, *J. Chem. Phys.*, 1988, **89**, 2193–2218.
38 G. A. Petersson and A.-L. Mohammad A, *J. Chem. Phys.*, 1991, **9**, 6081–6090.
39 H. Li, X. Wang, K. Yuan, L. Lv, K. Liu and Z. Li, *ACS Omega*, 2023, **8**, 17171–17180.
40 X. X. Li, M. X. Du, C. Y. Ma, W. K. Dong and Y. J. Ding, *J. Mol. Struct.*, 2024, **1295**, 136792.
41 Y. T. La, M. X. Du, L. L. Gan, Y. Zhang, Y. X. Sun and W. K. Dong, *Spectrochim. Acta, Part A*, 2024, **305**, 123481.
42 W. C. Chan, M. P. Ng, C. H. Tan, C. W. Ang, K. S. Sim, S. Y. X. Tiong, N. A. S. Pungut, C. H. Ng and K. W. Tan, *J. Photochem. Photobiol., A*, 2023, **436**, 114382.
43 M. Sahu, A. K. Manna, S. Chowdhury and G. K. Patra, *RSC Adv.*, 2020, **10**, 44860–44875.
44 X.-X. Li, C.-Y. Ma, M.-X. Du, W.-K. Dong and Y.-j. Ding, *J. Mol. Struct.*, 2024, **1299**, 137188.
45 F. Denizot and R. Lang, *J. Immunol. Methods*, 1986, **89**, 271–277.
46 B. K. Datta, D. Thiyagarajan, S. Samanta, A. Ramesh and G. Das, *Org. Biomol. Chem.*, 2014, **12**, 4975–4982.
47 B. Mohan, N. M. Kunhumon and S. Shanmugaraju, *Sens. Diagn.*, 2023, **2**, 1158–1175.